Composition and Control of a New Type of Hybrid Voltage-Source Converter Based on DRUs and FB-MMC for Large-Scale Offshore Wind Power Integration and Transmission

Chengdong Wang, *Student Member, IEEE*, Asif Ali, and Frede Blaabjerg, *Fellow, IEEE*

***Abstract*—The composition and control of a new type of hybrid voltage-source converters (H-VSCs) are proposed based on diode rectifier units (DRUs) and full-bridge modular multilevel converter (FB-MMC) to reduce the topside volume and weight of offshore wind farm (OWF) converter stations. The relationship between FB-MMC dc voltage ratio and its modulation index is presented to obtain the FB-MMC active power capacity. The equilibrium point is analyzed using numerical calculations. Then, a controller derived from proportional-integral controller is adopted to control FB-MMC dc voltage and a reactive power controller is added to balance the reactive power of OWF, FB-MMC and DRU, by which the PCC voltage is established for wind turbine converters grid access. In addition, the dc short-circuit fault and offshore short-circuit fault recovery strategy is also presented. Finally, two specific case parameters are calculated and a simulation model in RSCAD is developed to validate the effectiveness and feasibility of the topology as well as the proposed control strategy of the H-VSCs.**

***Index Terms*—Control strategy, dc voltage ratio, diode rectifier unit (DRU), fault recovery strategy, full-bridge modular multilevel converter (FB-MMC), hybrid voltage-source converter (H-VSC) composition, offshore wind power, reactive power balance.**

I. INTRODUCTION

IN RECENT years, energy transitions featuring carbon peaking and carbon neutrality have been proposed to achieve net zero emissions by many countries [1], [2], [3]. By all means, photovoltaic power and wind power have emerged as two effective ways of sustainable power generation [4], [5]. However, owing to the mismatch distribution between renewable energy resources and power loads in some countries, the high voltage alternate current (HVAC) and high voltage direct current (HVDC) transmission technologies have been developed with numerous projects already in operation or planned for the future. As a result, offshore wind power has attracted increasing interest due to its proximity to power load, reduced impact on humans in terms of acoustics and visuals [6], [7], [8], and the availability of strong and consistent sea winds, which means offshore wind turbine converters (WTCs) possess a much larger capacity factor and are capable of higher power generation compared to onshore WTCs. However, this imposes greater challenges in integration and transmission system due to the stringent requirements of the offshore constraints.

There are two approaches to power integration and transmission for offshore wind power [6], [7], [8]. In [9], it has been demonstrated that HVAC is economically more advantageous for near shore applications, while HVDC is more cost-effective and technically favorable for long-distance offshore scenarios. Among various HVDC solutions, modular multilevel converter-based HVDC (MMC-HVDC) has been the predominant option due to its well-known merits, such as the supporting capability of voltage and frequency for WTCs grid access [10], [11], [12], decoupling of active and reactive power [13], [14], [15], [16], [17], [18], modularity and scalability, low harmonics [19], [20], [21], [22], and ease of high voltage infrastructure [23], [24]. However, the large volume and weight of MMC converters present significant challenges for large-scale offshore wind power applications, such as in Gigawatt-level projects. The existing literature indicates that the diode rectifier units-based HVDC (DRU-HVDC) [9] has been put forward to significantly reduce the converter volume and weight. Although the DRU converter offers outstanding advantages in improvement of efficiency, reliability, and reduction of volume and weight, the control strategy of WTCs becomes more complicated than that in offshore wind farms (OWFs) connected by MMC-HVDC. In [25] and [26], a triple-loop active power control and quad-loop reactive power control, along with a phase-locked loop-based frequency control in a synchronous rotating frame, has been developed to coordinate individual grid side converters (GSCs) to establish ac collection system voltage and frequency. This control strategy implements proportional control of reactive

Manuscript received 14 April 2023; revised 5 October 2023 and 21 December 2023; accepted 1 February 2024. Date of publication 8 February 2024; date of current version 20 March 2024. Recommended for publication by Associate Editor E. Babaei. *(Corresponding author: Chengdong Wang.)*

Chengdong Wang is with the School of Electrical Engineering and Automation, Hefei University of Technology, Hefei 230009, China (e-mail: wangchengdong@mail.hfut.edu.cn).

Asif Ali is with the School of Electrical Engineering and Automation, Hefei University of Technology, Hefei 230009, China, and also with the Department of Electrical Engineering, Mehran University of Engineering and Technology, SZAB Campus, Khairpur 66020, Pakistan (e-mail: asif-solangi@mail.hfut.edu.cn).

Frede Blaabjerg is with the Department of Energy Technology, Aalborg University, DK-9220 Aalborg, Denmark (e-mail: fbl@et.aau.dk).

Color versions of one or more figures in this article are available at https://doi.org/10.1109/TPEL.2024.3363617.

Digital Object Identifier 10.1109/TPEL.2024.3363617

power and frequency to achieve synchronization and eliminate circulating current among different GSCs. In [27], a global positioning system-based synchronization and control strategy is employed to establish the voltage at the point of common coupling (PCC) for OWFs, ensuring the commutation of DRUs. Considering the hazardous offshore environment, the reliability and accuracy of communication are of concern for practical offshore wind power projects.

In general, the following functionalities are essential for OWFs connected by HVDC transmission.

1) *Establishment of PCC Voltage and Frequency:* In MMC-HVDC-connected OWFs, the MMC converter is capable of establishing the PCC voltage for WTCs grid access, whereas the GSCs are responsible to form the PCC voltage distributed and coordinated with the DRU-HVDC-connected ones.
2) *Active Power Regulation:* In MMC-HVDC-connected OWFs, the MMC converter increases its dc current to transmit more power while maintaining a constant PCC voltage. However, the PCC voltage needs to be varied to regulate the dc voltage and current in DRU-HVDC-connected OWFs.
3) *Dynamic Reactive power Balance:* For offshore wind power, the reactive power of GSCs, rectifier converter, and/or compensation equipment must be dynamically balanced to accommodate fluctuations in wind speed, i.e., wind power.
4) *Participation in Frequency Regulation of Onshore Power System*: With the energy pattern transition deploying, a new type of power system featuring a high penetration of renewable energy must be capable of implementing frequency regulation by renewable resources.
5) *Blocking DC Short-Circuit Fault Current:* For HVDC, the dc short-circuit fault is an obstacle because the dc current is not prone to be extinguished like ac current in HVAC.
6) *Black start capability:* During precharge and maintenance, the OWFs must be able to be energized by onshore power system, which indicates the power flow is inverse to normal operation.

To address the aforementioned functionalities and overcome the limitations of MMC-HVDC and DRU-HVDC, an alternate arm MMC is presented in [28], [29], [30], and [31]. However, the alternate arm still consists of series-connected semiconductor devices, originated from voltage-source converter-based HVDC (VSC-HVDC) known as HVDC light [32]. In [33], the concept of a parallel ac parallel dc hybrid topology is introduced to fully utilize the voltage supporting capability of MMC-HVDC and the higher efficiency of DRU-HVDC. However, this approach leads to a higher requirement of submodular (SM) quantity due to the MMC dc voltage being equal to the overall dc voltage. The authors of [34] carried out research to design a parallel ac series dc hybrid converter. However, the composition of the hybrid converter is not investigated. Furthermore, [35] presented a design methodology for a parallel ac series dc hybrid converter to establish a unidirectional transmission system for onshore bulk power transmission. However, this hybrid converter operates in current source mode, and the approach is not feasible for integrating offshore wind power due to the lack of voltage supporting capability.

In this article, the topology and control strategy of a new type of hybrid voltage-source converter (H-VSC) are proposed to address the limitations of both MMC-HVDC and DRU-HVDC. A topology with different dc voltage ratios and corresponding modulation indices is constructed to operate as one unified topology by parallel connection on ac side and series connection on dc side of full-bridge MMC (FB-MMC) and DRUs. Moreover, the FB-MMC assumes the responsibility of generating the PCC voltage, similar to MMC-HVDC. Bound as one converter via composition and control strategy, the hybrid converter of this topology exhibits the characteristics of a voltage-source converter from the perspective of the GSCs. Consequently, the aforementioned functionalities are obtained by the hybrid converter of this topology.

The contributions of the proposed article are summarized as follows.

1) The composition of the new topology is presented. The dc voltage ratio of FB-MMC is derived in details to make the hybrid converter to act as a voltage-source converter.
2) The FB-MMC reactive power capacity is proposed to balance the reactive power of OWFs and DRUs automatically.
3) The FB-MMC control strategy is interpreted to generate PCC voltage for GSC grid access so that the GSC can operate in traditional grid-following mode.
4) DC short-circuit fault and offshore short-circuit fault ride-through performances are validated.

The rest of this article is organized as follows. Section II depicts the hybrid converter composition from the relationship between FB-MMC active power ratio (i.e., dc voltage ratio) and its modulation index, and then the reactive power requirement is presented, and finally, the number of SMs is proposed. In Section III, the grid forming capability of the proposed hybrid converter is analyzed. In Section IV, a proportional-integral (PI) derivative controller is suggested to control FB-MMC dc voltage and to establish the PCC voltage, a PI controller is proposed to balance the reactive power. Also, a control strategy during the dc short-circuit fault and offshore short-circuit fault recovery is proposed to avoid reactive power overshoot. In Section V, a simulation model corresponding to two specific cases is built in RSCAD, and the results demonstrate the effectiveness and feasibility of the topology and control strategy. Section VI gives a comparison with other HVDC schemes and also a discussion on PCC voltage harmonics. Finally, Section VII concludes this article.

II. COMPOSITION OF H-VSC TOPOLOGY

The composition and control strategy of the H-VSC is depicted in Fig. 1. Each DRU unit consists of two 12-pulse diode rectifiers, two Y/y/d11 linking transformers, one high pass harmonic filter (HPF), and one thyristor switch. On the dc side, a low-capacity three-phase FB-MMC is connected in series with the DRU, while on the ac side, it is directly connected in parallel to the PCC bus. The adoption of the FB-MMC enables the converter to block the dc side pole-to-pole short-circuit current

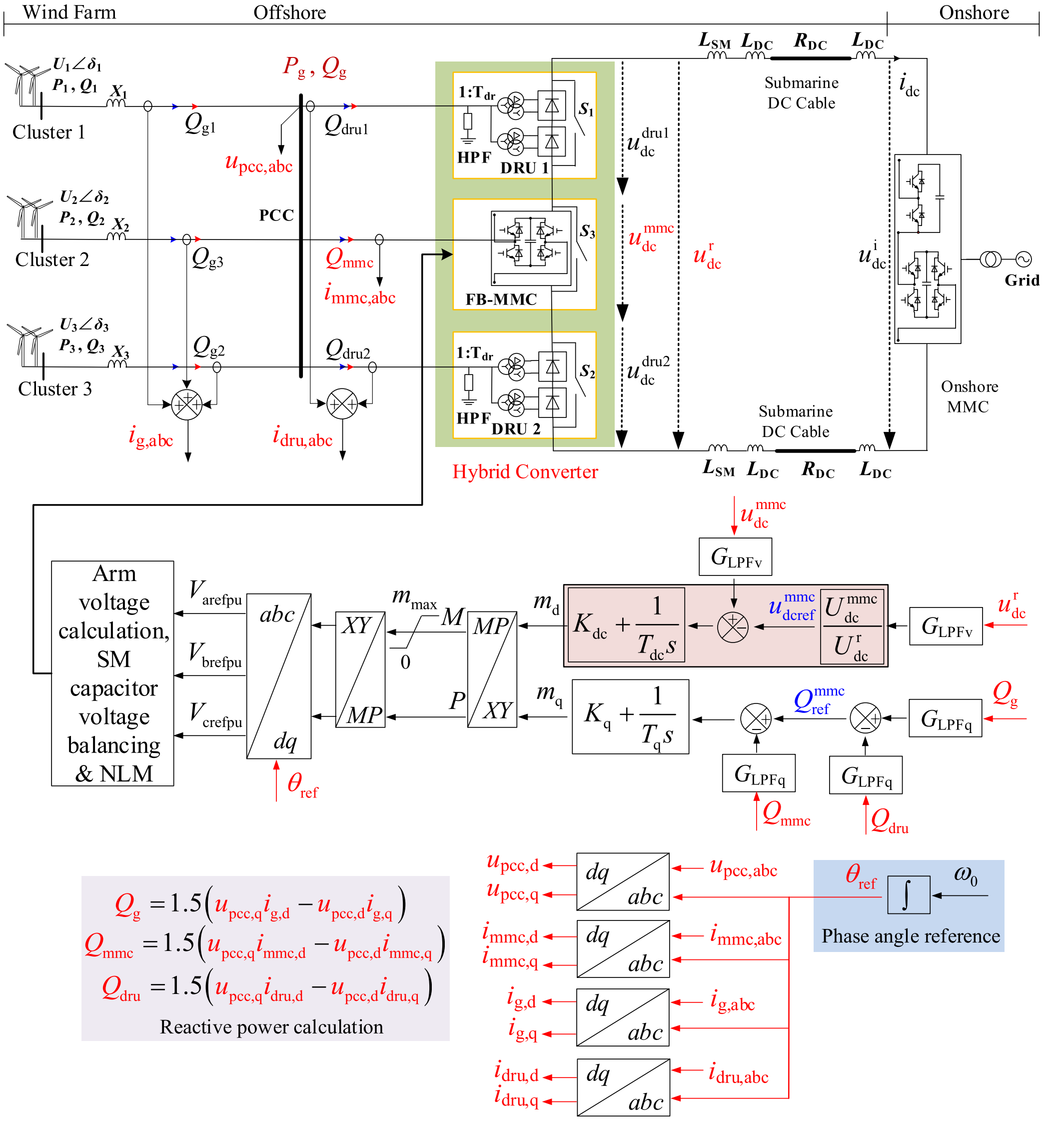

Fig. 1. Topology and control strategy of a new type of voltage-source converters for offshore wind farms.

obtained from the offshore side, which allows for a reduced leakage reactance of the DRU transformers compared to [31]. Meanwhile, the FB-MMC energizes the offshore network and GSCs dc link capacitors during precharge and maintenance by switching on the DRU thyristor switches S_1 and S_2 and switching OFF their ac side breakers. In this Section, the composition of the H-VSC is elaborated in details and its control strategy is analyzed in the following section.

A. Determination of FB-MMC DC Voltage Ratio

From Fig. 1, the dc voltage relationship can be expressed as

$$U_{\mathrm{dc}}^{\mathrm{r}} = U_{\mathrm{dc}}^{\mathrm{dru}} + U_{\mathrm{dc}}^{\mathrm{mmc}} \tag{1}$$

and

$$U_{\mathrm{dc}}^{\mathrm{dru}} = U_{\mathrm{dc}}^{\mathrm{dru1}} + U_{\mathrm{dc}}^{\mathrm{dru2}} \tag{2}$$

where U_{dc}^{r}, $U_{\mathrm{dc}}^{\mathrm{mmc}}$ and $U_{\mathrm{dc}}^{\mathrm{dru}}$ denote nominal dc voltage of the hybrid converter, FB-MMC, and DRU, respectively. $U_{\mathrm{dc}}^{\mathrm{dru1}}$ and $U_{\mathrm{dc}}^{\mathrm{dru2}}$ are nominal dc voltage of DRU 1 and DRU 2, respectively.

In this topology, it is challenging to predict whether the FB-MMC is capable to control the PCC voltage or not. Thus, the relationship between the FB-MMC active power ratio, i.e., FB-MMC dc voltage ratio, and its control ability of PCC voltage is interpreted in this section.

It is assumed that the FB-MMC is able to generate the PCC voltage for GSCs grid access for concise analysis. According to the modulation theory [36], the PCC line voltage is expressed by the FB-MMC dc voltage as

$$U_{\mathrm{ac}}^{\mathrm{mmc}} = \frac{U_{\mathrm{dc}}^{\mathrm{mmc}}}{2} m \frac{1}{\sqrt{2}} \sqrt{3} \tag{3}$$

where $U_{\mathrm{ac}}^{\mathrm{mmc}}$ and m are PCC line voltage (RMS) and modulation index, respectively. Then, the DRU dc voltage can be obtained

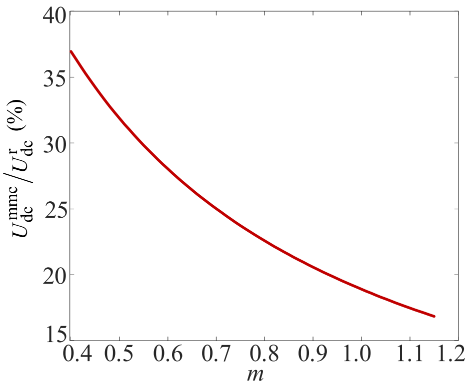

Fig. 2. MMC DC voltage ratio with modulation index m.

as

$$U_{\mathrm{dc}}^{dr}=K_b\left(\frac{3\sqrt{2}}{\pi}U_{\mathrm{ac}}^{\mathrm{mmc}}T_{dr}-\frac{3}{\pi}X_tI_{\mathrm{dc}}\right) \tag{4}$$

where K_b, T_{dr}, and X_t are the number of six-pulse diode rectifiers, linking transformer turns ratio and leakage reactance. I_{dc} denotes dc current and it can be expressed by total OWFs active power P_g as follows:

$$I_{\mathrm{dc}}=\frac{P_g}{U_{\mathrm{dc}}^r}. \tag{5}$$

From (1), the relationship among FB-MMC dc voltage, the total OWFs active power, and the hybrid converter dc voltage can be obtained as

$$\left(\frac{3\sqrt{3}}{2\pi}K_bT_{dr}m{+}1\right)U_{\mathrm{dc}}^{\mathrm{mmc}}=\frac{3}{\pi}X_tK_b\frac{P_g}{U_{\mathrm{dc}}^r}+U_{\mathrm{dc}}^r. \tag{6}$$

Choosing the hybrid converter dc voltage as a reference, the above equation can be rewritten as

$$\left(\frac{3\sqrt{3}}{2\pi}K_bT_{dr}m{+}1\right)\frac{U_{\mathrm{dc}}^{\mathrm{mmc}}}{U_{\mathrm{dc}}^r}=\frac{3}{\pi}X_tK_b\frac{P_g}{\left(U_{\mathrm{dc}}^r\right)^2}+1. \tag{7}$$

The factor $P_g/(U_{\mathrm{dc}}{}^r)^2$ of the first term on the right-hand side of equality sign is much less than 1 for the HVDC system. Therefore, the first term can be omitted and the relationship between FB-MMC dc voltage ratio δ and its modulation index m can be acquired. It is apparent that the FB-MMC dc voltage ratio is predominantly dependent on its modulation index, rather than on the OWFs active power and overall dc voltage. For a typical OWF with 66 kV integration cables, the number of 6-pulse diode rectifiers and linking transformer turn ratio can be designed to be 8 and 21.83 kV/66 kV as shown in Fig. 1 to enhance the hybrid converter reliability. With the above parameters, the relationship is illustrated in Fig. 2. Subsequently, when the modulation index is chosen, the SM number can be calculated as

$$N_1=\left(\frac{U_{\mathrm{dc}}^{\mathrm{mmc}}}{U_{\mathrm{dc}}^r}\right)\frac{U_{\mathrm{dc}}^r}{U_{\mathrm{SM}}} \tag{8}$$

where N_1 and U_{SM} are the SM number and rated voltage, respectively.

B. Determination of FB-MMC Reactive Power

The GSCs reactive power can be set to zero to efficiently utilize the converter capacity for OWFs. However, the GSCs step-up transformers and collecting cables also contribute to the overall reactive components. Furthermore, since the active power generated by the OWFs fluctuates with varying wind speeds, the reactive power of the DRU will vary correspondingly. Therefore, it is important to accurately calculate the maximum reactive power of the integration system through power flow analysis or electromagnetic simulation. Once the OWFs reactive power is determined, the FB-MMC reactive power can be obtained as

$$Q_{\mathrm{mmc}}=Q_g-Q_{dr} \tag{9}$$

where Q_{mmc}, Q_g, and Q_{dr} are, respectively, reactive power of FB-MMC, OWFs, and DRU. Considering the power flow analysis is beyond the scope of this article, the reactive power will be obtained by RTDS real-time simulations in Section V.

C. SM Count Requirement for DC Short-Circuit Fault Ride-Through

The FBSM dc voltage polarity can be inverted by a proper control. Consequently, in the event of a dc short-circuit fault, the FB-MMC is utilized to suppress dc current by blocking all SMs to prevent potential damage of the semiconductor devices and cables. Additionally, a distributed energy storage system based on supercapacitors is installed at the WTCs' dc link to serve the purpose of absorbing surplus power during dc short-circuit faults and participating in the onshore frequency regulation. As a result, the FB-MMC SM count can be determined by considering the complete transfer of magnetic field energy from the smoothing reactor and equivalent dc cable reactor into the electric field energy of the SM capacitors as follows:

$$\begin{aligned}2*\frac{1}{2}L_{\sum}\left(I_{\mathrm{dc}}^{\max}\right)^2&=\frac{1}{2}C_{\mathrm{SM}}\left(K_{ov}U_{\mathrm{SM}}\right)^2*\left(6N_2\right)\\&\quad-\frac{1}{2}C_{\mathrm{SM}}\left(U_{\mathrm{SM}}\right)^2*\left(6N_2\right)\end{aligned} \tag{10}$$

where L_{Σ}, C_{SM}, K_{ov}, and $I_{\mathrm{dc}}^{\max}$ are total equivalent reactance, SM capacitance, SM overvoltage index, and dc overcurrent threshold, respectively. Subsequently, the SM count N_2 can be expressed as

$$N_2=\frac{L_{\sum}\left(I_{\mathrm{dc}}^{\max}\right)^2}{3C_{\mathrm{SM}}\left(U_{\mathrm{SM}}\right)^2\left(\left(K_{ov}\right)^2-1\right)}. \tag{11}$$

Considering both FB-MMC dc voltage ratio and dc fault ride-through requirement, the FB-MMC SM count N can be chosen as the largest one, mathematically given as

$$N=\max\left(N_1,N_2\right). \tag{12}$$

III. HYBRID CONVERTER GRID FORMING CAPABILITY ANALYSIS

To analyze the equilibrium point of the hybrid converter presented in Section II, the ac side equivalent circuit is obtained

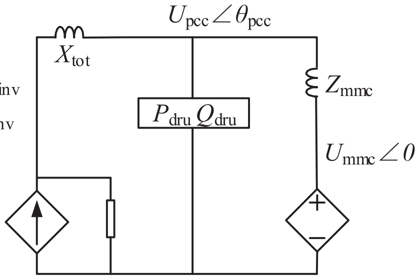

Fig. 3. Equivalent circuit of OWF AC side.

as shown in Fig. 3, where X_{tot} denotes the total impedance of GSC step-up transformer and transmission cable, U_{mmc}, U_{pcc}, and U_{inv} denote the voltage magnitude of FB-MMC ac side, PCC, and the GSC output side, θ_{pcc} and θ_{inv} denote the voltage phase angle with respect to FB-MMC ac side voltage, and I_{inv} denotes the GSC output current. To simplify the analysis, the following assumptions are made as follows.

1) The grid-following converter operates at unity power factor; thus, it is represented by a controlled current source with only the terminal voltage and current focused in the equivalent model.
2) The PCC voltage is established by the FB-MMC; thus, the FB-MMC is represented by a controlled voltage source with only its terminal voltage (phase voltage) focused and chosen as a reference. $Z_{mmc}= j\omega_0 \frac{L_{arm}}{2}$ reflects the equivalent arm inductance at the power frequency.

From Fig. 3, the complex power of DRU and MMC can be given as

$$3U_{pcc}e^{j\theta_{pcc}}\overline{\left(I_{inv}e^{j\theta_{inv}}-\frac{\left(U_{pcc}e^{j\theta_{pcc}}-U_{mmc}e^{j0}\right)}{Z_{mmc}}\right)} = P_{dru}+jQ_{dru} \tag{13}$$

and

$$3U_{pcc}e^{j\theta_{pcc}}\overline{\left(\frac{U_{pcc}e^{j\theta_{pcc}}-U_{mmc}e^{j0}}{Z_{mmc}}\right)} = P_{mmc}+jQ_{mmc} \tag{14}$$

where the bar represents conjugate operation, P_{dru} and P_{mmc} denote the active power of DRU and FB-MMC, respectively, Q_{dru} and Q_{mmc} denote the reactive power of DRU and FB-MMC, respectively. Therefore, the active power of DRU and MMC can be obtained as

$$3U_{pcc}I_{inv}\cos\left(\theta_{pcc}-\theta_{inv}\right)-\frac{3U_{pcc}U_{mmc}\sin\theta_{pcc}}{|Z_{mmc}|} = P_{dru} \tag{15}$$

and

$$\frac{3U_{pcc}U_{mmc}\sin\theta_{pcc}}{|Z_{mmc}|} = P_{mmc} \tag{16}$$

which leads to

$$-1+\frac{|Z_{mmc}|\,I_{inv}\cos\left(\theta_{pcc}-\theta_{inv}\right)}{U_{mmc}\sin\theta_{pcc}} = \frac{P_{dru}}{P_{mmc}}. \tag{17}$$

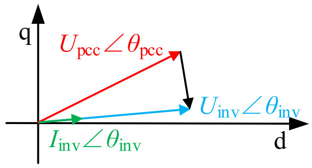

Fig. 4. Relationship between voltage vectors of GSC and PCC.

It is well known that, for a rectifier, the ac side active power is equal to its dc side power [37], which means

$$P_{dru} = U_{dc}^{dru}I_{dc} \tag{18}$$

and

$$P_{mmc} = U_{dc}^{mmc}I_{dc}. \tag{19}$$

From (18) and (19), the active power ratio can be represented by a voltage ratio as follows:

$$\frac{U_{dc}^{r}-U_{dc}^{mmc}}{U_{dc}^{mmc}} = \frac{P_{dru}}{P_{mmc}}. \tag{20}$$

Based on (17) and (20), the following expression can be obtained:

$$-1+\frac{|Z_{mmc}|\,I_{inv}\cos\left(\theta_{pcc}-\theta_{inv}\right)}{U_{mmc}\sin\theta_{pcc}} = \frac{1-\frac{U_{dc}^{mmc}}{U_{dc}^{r}}}{\frac{U_{dc}^{mmc}}{U_{dc}^{r}}}. \tag{21}$$

It is clear from (21) that the power angle of PCC, θ_{pcc}, depends on the phase difference of voltage of PCC and GSC. The dc voltage ratio is determined by the composition in Section II. On the other hand, the following conclusion can be obtained by adding (15) into (16)

$$P_g = 3U_{pcc}I_{inv}\cos\left(\theta_{pcc}-\theta_{inv}\right) \tag{22}$$

which indicates that the power angle achieves its maximum value $\theta_{pcc,max}$ at the maximum OWF active power, i.e., when the product of the cosine of the phase difference and GSC current achieves the maximum value.

According to the assumption at the beginning of this section, the relationship between voltage vectors of GSC and PCC, as shown in Fig. 4, can be expressed as follows:

$$U_{pcc}e^{j\theta_{pcc}}-jX_{tot}I_{inv}e^{j\theta_{inv}} = U_{inv}e^{j\theta_{inv}} \tag{23}$$

which can be rewritten as

$$\begin{cases} U_{pcc}-I_{inv}X_{tot}\sin\left(\theta_{pcc}-\theta_{inv}\right) = U_{inv}\cos\left(\theta_{pcc}-\theta_{inv}\right) \\ I_{inv}X_{tot}\cos\left(\theta_{pcc}-\theta_{inv}\right) = U_{inv}\sin\left(\theta_{pcc}-\theta_{inv}\right) \end{cases} \tag{24}$$

leading to

$$\frac{U_{pcc}}{I_{inv}\cos\left(\theta_{pcc}-\theta_{inv}\right)X_{tot}} = \tan\left(\theta_{pcc}-\theta_{inv}\right)+\frac{1}{\tan\left(\theta_{pcc}-\theta_{inv}\right)}. \tag{25}$$

It can be seen from Fig. 4 that the phase difference achieves its maximum, $(\theta_{pcc}\text{-}\theta_{inv})_{max}$, at the maximum GSC current (1.1 p.u. in this article), which coincide with the maximum OWF

TABLE I
NUMERICAL CALCULATION RESULTS OF EQUILIBRIUM POINT

DC voltage ratio	$U_{\rm mmc}$ (p.u.)	$U_{\rm pcc}$ (p.u.)	$I_{\rm inv}$ (p.u.)	($\theta_{\rm pcc}$-$\theta_{\rm inv}$) (°)	$\theta_{\rm pcc}$ (°)
0.33	1.20	0.94	1.09	9.13	15.45
0.22	1.22	0.95	1.08	15.03	14.56

TABLE II
SYSTEM PARAMETERS

Components	Parameters	Values
HVDC link	Power	1200 MW
	DC voltage	640 kV
	DC cable length	200 km
Onshore MMC	Submodule capacitance	10 mF
	Submodule number per arm	320
	Submodule capacitor voltage	2 kV
	Arm inductance	29 mH
	Transformer (Y/Δ)	380/220 kV
	Leakage reactance	0.18 p.u.
FB-MMC	Submodule capacitance	10 mF
	Submodule capacitor voltage	2 kV
	Arm inductance	29 mH
Smoothing Reactor	$L_{\rm SM}$	0.12 H
Onshore MMC Control Parameters (p.u.)	Current control: $K_{\rm i}$; $T_{\rm i}$	0.48; 0.0067
	DC voltage control: $K_{\rm dc}$; $T_{\rm dc}$	8.0; 0.00267
	Q control: $K_{\rm q}$; $T_{\rm q}$	0.48; 0.0303
FB-MMC Control Parameters (p.u.)	DC voltage control: $K_{\rm dc}$; $T_{\rm dc}$	0.1; 0.075
	$G_{\rm LPFv}$ cutoff frequency and damping ratio	16 Hz; 0.7
	Q control: $K_{\rm q}$; $T_{\rm q}$	0.25; 0.2
	$G_{\rm LPFq}$ cutoff frequency and damping ratio	140 Hz; 0.7

active power. Meanwhile, the reactive power of DRU and FB-MMC can be obtained from (13) and (14) as

$$3U_{\rm pcc}I_{\rm inv}\sin\left(\theta_{\rm pcc}-\theta_{\rm inv}\right)-\frac{3U_{\rm pcc}\left(U_{\rm pcc}-U_{\rm mmc}\cos\theta_{\rm pcc}\right)}{|Z_{\rm mmc}|}=Q_{\rm dru} \tag{26}$$

and

$$\frac{3U_{\rm pcc}\left(U_{\rm pcc}-U_{\rm mmc}\cos\theta_{\rm pcc}\right)}{|Z_{\rm mmc}|}=Q_{\rm mmc}. \tag{27}$$

Based on (21), (22), (25), (26), and (27), the voltage magnitudes of FB-MMC $U_{\rm mmc}$ and PCC $U_{\rm pcc}$, GSC output current $I_{\rm inv}$, phase difference ($\theta_{\rm pcc}$-$\theta_{\rm inv}$), and the power angle $\theta_{\rm pcc}$ are obtained by numerical calculations under the conditions of maximum GSC current (1.1 p.u.) and specific FB-MMC dc voltage ratios. In this article, two cases with FB-MMC dc voltage ratios of 0.32 and 0.22 are studied and the results are given in Table I with system parameters given in Table II. It can be seen from Table I that the power angle of PCC is relatively small, and the voltage magnitude of FB-MMC $U_{\rm mmc}$ falls within the range of the maximum FB-MMC output voltage for both scenarios (107 kV at dc voltage ratio of 0.33 and 70 kV at dc voltage ratio of 0.22), which indicates the FB-MMC is capable to form the offshore grid for the GSC grid access. In other words, there exists an equilibrium point for the hybrid converter [38].

IV. CONTROL STRATEGY OF THE HYBRID CONVERTER

A. *Control Strategy for Normal Operation*

In normal operating condition, the hybrid converter is responsible for transmitting the varying and random OWF power to onshore. On the other hand, the power balancing regulation between FB-MMC and DRU is also necessary to avoid long-time overload of the FB-MMC or DRUs. From the composition process, it can be concluded that the instantaneous FB-MMC dc voltage must be controlled in accordance with its dc voltage ratio. Thus, a proportional and integral controller can be adopted to control the FB-MMC dc voltage with its reference generated by multiplying the overall dc voltage and the dc voltage ratio as shown in Fig. 1, where $u_{\rm dc}^{r}$ and $u_{\rm dc}^{\rm mmc}$ are instantaneous dc voltages of the hybrid converter and FB-MMC, $u_{\rm dcref}^{\rm mmc}$ is the reference of dc voltage controller with proportional coefficient $K_{\rm dc}$ and integral coefficient $T_{\rm dc}$, and m_d is the d-axis component of the modulation index. Meanwhile, to balance the OWF reactive power Q_g, DRU reactive power $Q_{\rm dru}$, and FB-MMC reactive power $Q_{\rm mmc}$, a PI controller with proportional coefficient K_q and integral coefficient T_q can be added to generate the q-axis component m_q of the modulation index. Two second-order low-pass filters $G_{{\rm LPF}\,v}$ and $G_{{\rm LPF}\,q}$ are embedded in their respective loops to filter out the high frequency components of dc voltage and reactive power. Transformations from Cartesian coordinate system to polar coordinate system and its inverse are added to limit the magnitude of modulation index with its upper limit $m_{\rm max}$. ω_0 and $\theta_{\rm ref}$ are PCC voltage angular frequency and phase angle, and $V_{\rm arefpu}$, $V_{\rm brefpu}$, and $V_{\rm crefpu}$ are the three-phase modulation signals. The PCC voltage $u_{{\rm pcc},abc}$, OWF current $i_{g,abc}$, DRU current $i_{{\rm dru},abc}$, and FB-MMC current $i_{{\rm mmc},abc}$ are transformed from *abc* reference frame to *dq* reference frame based on the phase angle $\theta_{\rm ref}$ to obtain the reactive power of OWF, DRU, and FB-MMC. With this control strategy, the active powers of FB-MMC and DRU are automatically regulated to the expected values indicated by the dc voltage ratio.

B. *Control Strategy of Fault Recovery*

During fault recovery, it is vital for the FB-MMC to reestablish the PCC voltage for resuming the power transmission. However, excessively rapid recovery may result in a reactive power overshoot, which could be even larger than FB-MMC capacity, therefore a proper upper limit of modulation index m is necessary. Since it is difficult to calculate the transient reactive power accurately, a trial-and-error approach is taken to obtain a reasonable modulation index value of 0.4 to avoid overshoot during fault recovery. With this limitation, the PCC voltage is slightly lower than the starting voltage, at which the offshore dc voltage $u_{\rm dc}^{r}$ begins to exceed the onshore dc voltage $u_{\rm dc}^{i}$, so that the active and reactive power can be recovered without

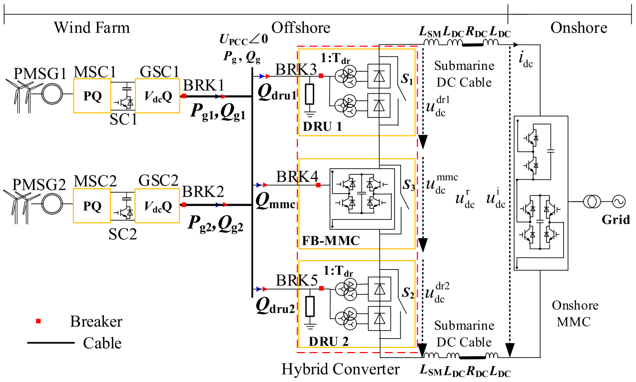

Fig. 5. Simulation model of the offshore wind farm integration and transmission system.

significant overshoot during the period when they are ramping up to its rated value.

V. Simulation Verification

To verify the feasibility of the topology and control strategy, a complete OWF model with the parameters given in Table II is built in RTDS real-time platform. Since the offshore grid is weak, the permanent magnet synchronous generator (PMSG) and fully rated converter (FRC) are adopted with parameters referred as sample case“MMC offshore wind” from PSCAD knowledge base [39]. A dc chopper resistor of 100 Ω is installed in the FB-MMC dc side to dissipate surplus power to avoid SM capacitor overvoltage during dc short-circuit fault especially when the SM number is small. The hysteresis control upper threshold of cutting in is 1.15 p.u., and lower threshold of cutting OFF is 0.85 p.u. From the perspective of verifying the functionality of the hybrid converter, the GSC output currents are magnified by a factor of 120. In addition, a supercapacitor rated at 864 V and 27.5 F is installed in the FRC dc link to store surplus power at fault conditions and participate in the onshore frequency regulation, as shown in Fig. 5.

Two cases of the FB-MMC capacity are considered. First, the SM number N_2 can be obtained as 13 from (11) with total equivalent reactance of 0.14 H, SM capacitance of 10 mF, SM overvoltage index of 1.5, dc overcurrent threshold of 4 kA, and rated SM capacitor voltage of 2 kV. Second, two modulation indices of 0.51 and 0.77 are chosen to validate the effectiveness of the hybrid converter composition. For the former modulation index, it can be obtained from (7) that the dc voltage ratio is 0.33, thus FB-MMC dc voltage is 213 kV and DRU transformer ratio is 87.3 kV/66 kV. Furthermore, the SM number N_1 is 107. For the latter case, the four parameters are 0.22, 140 kV, 102.5 kV/66 kV, and 70, respectively. Accordingly, the HPF parameters of DRU are 1.19 Ω, 1.56 mH, and 58.49 uF when the dc voltage ratio is 0.33 and 1.01 Ω, 1.32 mH and 69.13 uF when the dc voltage ratio is 0.22.

A. Verification of Equilibrium Point

To verify the existence of an equilibrium point for the hybrid converter, the breaker BRK2 in Fig. 5 is switched OFF and the current magnifying factor is set to be 240 to generate 1200 MW of OWF active power. The voltage magnitudes of FB-MMC U_{mmc} and PCC U_{pcc}, GSC output current I_{inv}, phase difference (θ_{pcc}-θ_{inv}), and the power angle θ_{pcc} are tested and given in Table III based on fast Fourier transform. It can be seen that the voltages and angles agree well with the numerical calculations results in Table I for both cases, indicating the existence of an equilibrium point of the hybrid converter.

TABLE III
Experimental Results of Equilibrium Point

DC voltage ratio	U_{mmc} (p.u.)	U_{pcc} (p.u.)	I_{inv} (p.u.)	(θ_{pcc}-θ_{inv}) (°)	θ_{pcc} (°)
0.33	1.19	0.95	1.08	9.26	15.35
0.22	1.20	0.96	1.05	14.46	14.38

TABLE IV
Start-Up Procedure

Time	Events
0	All breakers are switched off. S_1 and S_2 are switched ON. S_3 is switched OFF.
0.1 s	BRK1 and BRK4 are switched on. Onshore MMC starts at one-third of rated dc voltage to precharge FB-MMC and GSC1 dc capacitor.
0.3 s	S_1 and S_2 are switched OFF. BRK3 and BRK5 are switched ON.
1.25 s	GSC1 starts to ramp up to rated power.
1.95 s	GSC2 starts to ramp up to rated power.

B. Power Regulation Performance

The system responses to OWF power variation under modulation indices of 0.51 and 0.77 are illustrated in Fig. 6. The variables are distinguished from their counterparts with identifier “_213” and “_140” in their names in the two cases to validate. The start-up procedure is given in Table IV. After the OWF power reaches rated level, the motor side converter power reference is set to be 1.1, 0.9, 0.7, 0.5, 0.3, 0.1, 0.2, 0.4, 0.6, 0.8, and 1.0 p.u. at 3, 4, 5, 6, 7, 8, 9, 10, 11, 12, and 13 s, respectively. The ac and dc side instantaneous powers of the DRU and FB-MMC are illustrated in Fig. 6(a), from which it can be seen that the OWF active power is almost identical in the two cases and varies with references, but the active power of FB-MMC is 396 MW for a modulation index of 0.51 and 261 MW for a modulation index of 0.77, and the active powers of both DRU 1 and DRU 2 are 380 and 450 MW, respectively, in the two cases. The dc voltage of DRU and FB-MMC is shown in Fig. 6(b). It can be seen that the dc voltage of FB-MMC is 213 and 140 kV for modulation indices of 0.51 and 0.77 and the dc

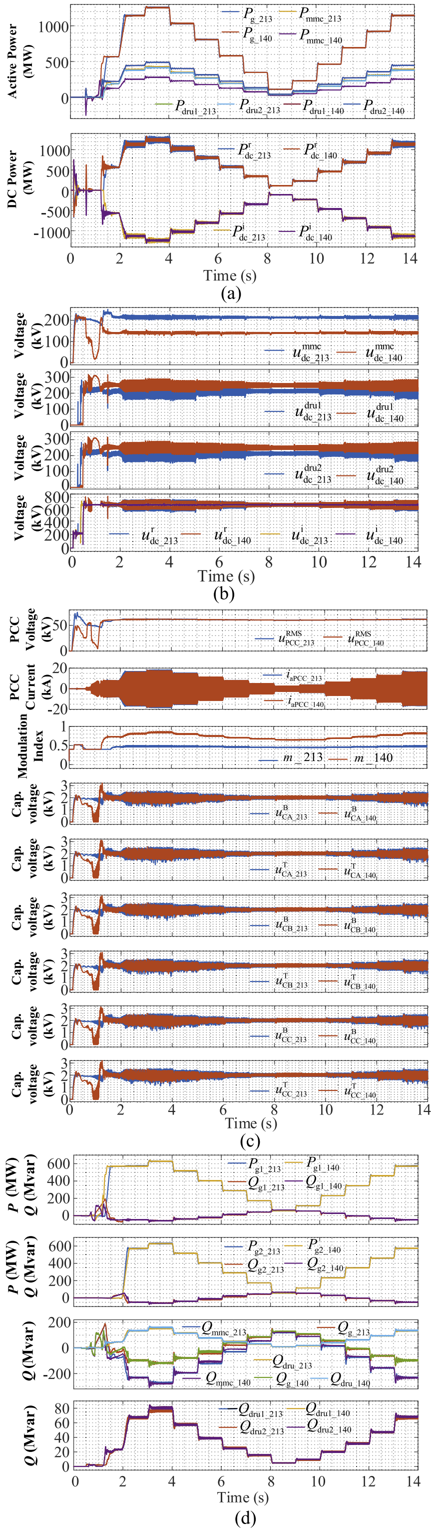

Fig. 6. Real time simulation power regulation waveforms for modulation indices of 0.51 and 0.77 for the H-VSC. (a) OWF active power P_g, FB-MMC active power P_{mmc}, DRU 1 active power P_{dru1}, DRU 2 active power P_{dru2}, offshore DC power P^r_{dc} and onshore DC power P^i_{dc}. (b) FB-MMC DC voltage $u^{\mathrm{mmc}}_{\mathrm{dc}}$, DRU 1 DC voltage $u^{\mathrm{dr1}}_{\mathrm{dc}}$, DRU 2 DC voltage $u^{\mathrm{dr2}}_{\mathrm{dc}}$, offshore DC voltage u^r_{dc}, and onshore DC voltage u^i_{dc}. (c) PCC RMS voltage $u^{\mathrm{RMS}}_{\mathrm{PCC}}$, phase A current of PCC i_{aPCC}, modulation index, Y (T means top and B means bottom) arm SM capacitor voltage of phase X ($X =$ A, B, C) u^Y_{CX}. (d) OWF 1 active power P_{g1} and reactive power Q_{g1}, OWF 2 active power P_{g2} and reactive power Q_{g2}, FB-MMC reactive power Q_{mmc}, OWF reactive power Q_g, total DRU reactive power Q_{dru}, DRU 1 reactive power Q_{dru1} and DRU 2 reactive power Q_{dru2}.

voltage of the DRU for a modulation index of 0.51 is higher than that of 0.77. The modulation indices and SM capacitor voltages are presented in Fig. 6(c). It is observed that the modulation index is slightly influenced by the OWF active power; that is, the average modulation index is 0.46 at active power of 1.0 p.u. and 0.44 at active power of 0.1 p.u. when the modulation index is designed to be 0.51, and 0.8 at active power of 1.0 p.u. and 0.71 at active power of 0.1 p.u. when it is designed to be 0.77. Meanwhile, all the SM capacitor voltages are well controlled at a targeted value of 2 kV. The results show that the hybrid converter is capable of integrating and transmitting variable OWF power with smooth and rapid responses for power step changes to the full power range. The PCC voltage harmonics are given in Table V with and without HPFs installed in the DRU. It is shown that the PCC voltage harmonics are acceptable in the full power range for both cases when the HPFs are installed in the system.

C. Fault Ride-Through Performance

The ride-through performances of a dc short-circuit fault and an offshore short-circuit fault with modulation indices of 0.51 and 0.77 are illustrated in Fig. 7. The system operates at a rated state to verify the fault ride-through performances before the dc short-circuit fault and the offshore short-circuit fault occur.

The dc short-circuit fault is triggered at 5 s and then maintained for 200 ms. It can be seen from Fig. 7(e) that after 1.2 ms of fault occurrence (2.2 ms under modulation index of 0.77), the dc current jumps up to an overcurrent threshold of 4 kA, and the FB-MMC is blocked immediately. Simultaneously, the dc chopper is activated to dissipate part of the surplus power to avoid SM capacitor overvoltages, which can be observed from Fig. 7(c). For the FRC, the supercapacitor is cut in as long as the dc voltage is higher than 1.2 p.u. After the dc short-circuit state disappears, the FB-MMC reestablishes the PCC voltage for GSCs grid access.

It is observed from Fig. 7(a) and (b) that there exists no severe overshoot of the active power and voltage during the dc short-circuit fault under the modulation index limit of 0.4. The results during dc short-circuit fault demonstrate a good performance of the hybrid converter.

The offshore short-circuit fault is triggered at 7 s and then maintained for 100 ms. With the supercapacitor cutting in and the PMSG deloading, the surplus power is transferred to the supercapacitor to avoid a WTC dc link overvoltage. After the offshore short-circuit fault disappears, the GSCs resynchronize to the PCC voltage to resume the power transmission. It is observed that the active power and voltage overshoot is very light during the offshore short-circuit fault, and the hybrid converter is capable to reestablish the PCC voltage for GSCs grid access as quickly as possible.

D. Dynamical Reactive Power Balance Performance

The reactive power balance among OWFs, DRUs, and FB-MMC can be well implemented with the control strategy proposed in Figs. 6(d) and 7(d). Although the GSCs reactive power reference is set to zero to facilitate the active power output, the cables' distributed capacitance and step-up transformers'

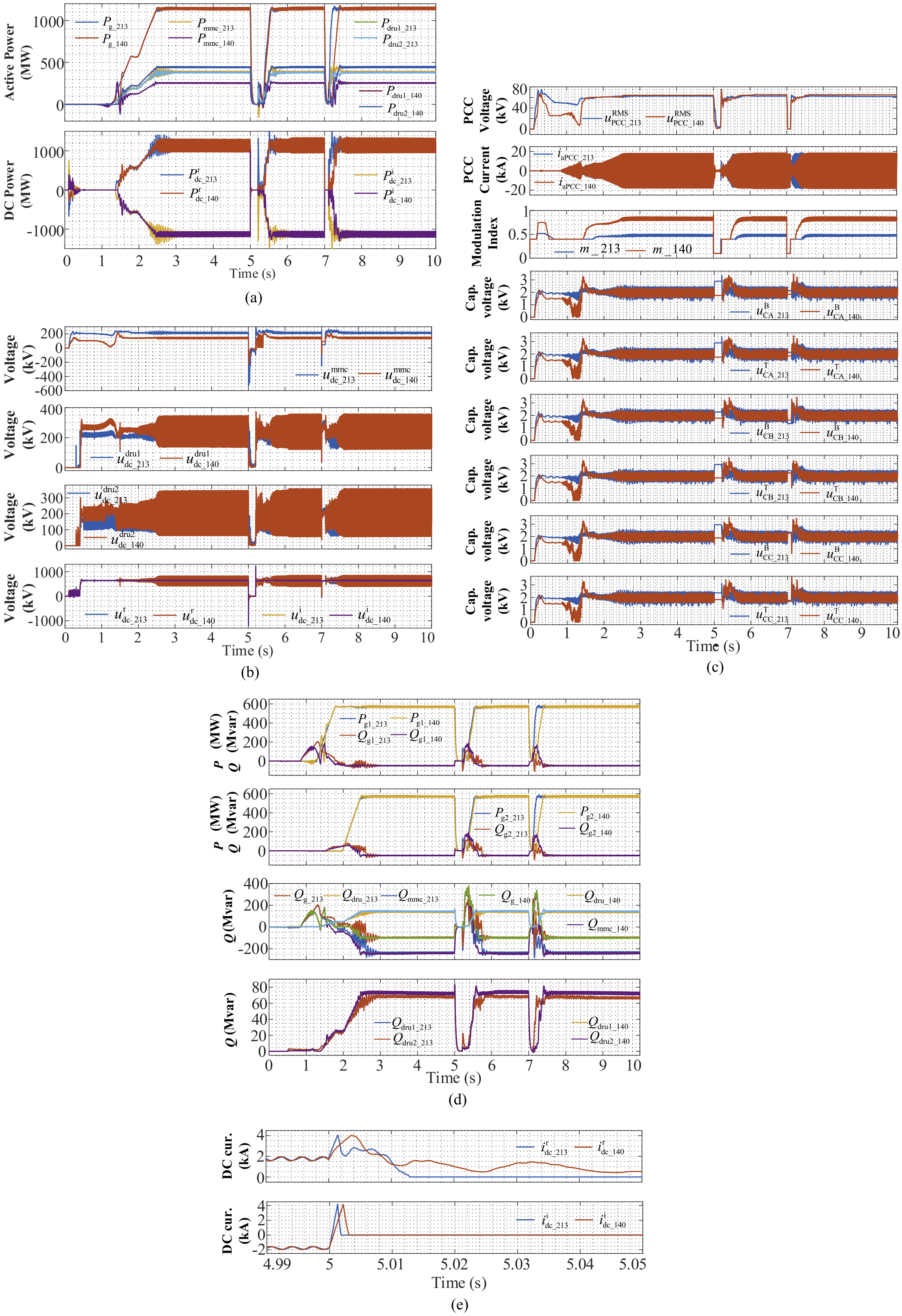

(a)

(b)

(c)

(d)

(e)

Fig. 7. Fault ride-through waveforms for modulation indices of 0.51 and 0.77 for the H-VSC. (a) OWF active power P_g, FB-MMC active power P_{mmc}, DRU 1 active power P_{dru1}, DRU 2 active power P_{dru2}, offshore DC power P^r_{dc} and onshore DC power P^i_{dc}. (b) FB-MMC DC voltage $u^{\mathrm{mmc}}_{\mathrm{dc}}$, DRU 1 DC voltage $u^{\mathrm{dru1}}_{\mathrm{dc}}$, DRU 2 DC voltage $u^{\mathrm{dru2}}_{\mathrm{dc}}$, offshore DC voltage u^r_{dc}, and onshore DC voltage u^i_{dc}. (c) PCC RMS voltage $u^{\mathrm{RMS}}_{\mathrm{PCC}}$, phase A current of PCC $i_{a\mathrm{PCC}}$, modulation index, Y (T means top and B means bottom) arm SM capacitor voltage of phase X ($X = $ A, B, C) u^Y_{CX}. (d) OWF 1 active power P_{g1} and reactive power Q_{g1}, OWF 2 active power P_{g2} and reactive power Q_{g2}, FB-MMC reactive power Q_{mmc}, OWF reactive power Q_{g}, total DRU reactive power Q_{dru}, DRU 1 reactive power Q_{dru1} and DRU2 reactive power Q_{dru2}. (e) Offshore DC current i^r_{dc} and onshore DC current i^i_{dc} during the DC short-circuit fault.

TABLE V
PCC VOLTAGE HARMONICS OF OFFSHORE WIND FARMS WITH AND WITHOUT HPF

Power (p.u.)	0.1	0.2	0.3	0.4	0.5	0.6	0.7	0.8	0.9	1.0	1.1
THD with HPF at mod. index of 0.51 (%)	0.42	0.74	0.99	1.25	1.47	1.68	1.89	2.11	2.37	2.85	3.01
THD with HPF at mod. index of 0.77 (%)	0.40	0.62	0.88	1.09	1.24	1.43	1.56	1.75	1.83	1.96	2.03
THD without HPF at mod. index of 0.51 (%)	2.72	4.56	4.21	6.22	8.18	7.06	5.39	7.42	8.06	8.41	5.59
THD without HPF at mod. index of 0.77 (%)	1.50	2.34	3.11	3.82	4.17	4.51	4.92	5.72	6.54	6.86	7.54

reactance are also reactive components. It can be seen that the OWF reactive power is around -92 and -113 Mvar, the DRU reactive power is around 160 and 150 Mvar, and the FB-MMC reactive power is -282 and -274 Mvar for modulation indices of 0.51 and 0.77 in the rated active power operating state. During the dc short-circuit recovery, the OWFs reactive power peaks are 246 and 367 Mvar, and the FB-MMC reactive power peaks are also 246 and 367 Mvar for the modulation indices of 0.51 and 0.77. During the offshore short-circuit recovery, the OWFs reactive power peaks are 263 and 323 Mvar, and the FB-MMC reactive power peaks are 142 and 312 Mvar for modulation indices of 0.51 and 0.77. The above waveforms prove a good dynamical reactive power balance performance of the hybrid converter.

VI. DISCUSSION

A. Comparisons With Other HVDC Schemes

According to [35], the loss in a converter station is primarily attributed to the semiconductors in the converter, transformers, converter reactors, dc reactors, and auxiliary supplies. Additionally, [35] provides a detailed breakdown of the different losses, revealing that the total loss in a FB-MMC amounts to 1.08%. With the DRU loss of 0.5% [35], the H-VSC loss ε at rated operation can be given as

$$\varepsilon = 1.08\% \times \delta + 0.5\% \times (1 - \delta) = 0.58\% \times \delta + 0.5\%$$

which demonstrates that the H-VSC has a higher efficiency than the FB-MMC but a lower efficiency than the DRU, and the efficiency decreases in proportion to the FB-MMC dc voltage ratio δ.

On the other hand, the commonly adopted metrics for the evaluation of power electronic systems encompass reliability, failure rate, mean time to failure, mean time to repair, and availability [40], [41]. The CIGRE conducts statistical works on HVDC project reliability [42], [43], [44]. The base failure rate of a FB-MMC module, including insulated gate bipolar transistor, capacitor, SM control, SM power supply, cooling, sensing subsystem, thyristor, bypass switch and its control, is developed in details in [45], [46], [47], [48], and [49] and it can be obtained as $2700/10^9$ hours. What's more, a reliable communication subsystem is necessary for MMC converter. However, the base failure rate of DRU can be referred to as $1020/10^9$ hours at most for its well-known simplicity [50], [51]. Therefore, the H-VSC has a lower failure rate than the FB-MMC, but a higher failure rate than the DRU without consideration of the redundancy level, which is similar to the efficiency. Meanwhile, the control strategy of GSCs can be completely identical for the OWFs connected by HVDC based on H-VSC (H-VSC-HVDC) and MMC-HVDC, whereas the control strategy of DRU-HVDC connected GSCs is more complicated than that of H-VSC-HVDC and MMC-HVDC connected ones. In a future work, the reliability analysis of DRU-HVDC, MMC-HVDC, and H-VSC-HVDC connected OWF systems, including GSCs and transmission link with different redundancy level, will be quantitatively developed to provide a guide for future OWF projects [52].

Additionally, the H-VSC-HVDC possesses the same frequency supporting capability as MMC-HVDC, which is of great importance for a new type power system dominated by high penetration renewable energy.

B. PCC Voltage Harmonics

The highest PCC voltage harmonic is 8.41%, which is higher than the allowable limit (5% in IEEE Std. 519-2022 [53]), but not too much higher, if a HPF is not installed near DRU. However, the simulation results prove that the OWF integration and transmission system can operate smoothly. Therefore, H-VSC-HVDC in absence of a HPF is a viable way out for the operating mode of OWFs in addition to MMC-HVDC and DRU-HVDC, thanks to the isolation function of the dc link compared with HVAC solutions; and it is thus proposed in this article.

VII. CONCLUSION

The composition and control strategy of a new type of H-VSC for OWF integration and transmission have been proposed in this article. By series connection of FB-MMC and DRU on the dc side and parallel connection on the ac side, the composition of the hybrid converter is constructed. The relationship between FB-MMC dc voltage ratio and its modulation index is discussed to acquire the FB-MMC active power capacity, and the reactive power capacity is obtained by simulation. The equilibrium point of the hybrid converter is given by numerical calculations. A simple and effective control strategy based on PI controller is able to automatically dispatch the designed ratio of the active power to the FB-MMC. Two groups of specific case parameters are calculated and time-domain simulations in the RSCAD real-time platform demonstrate that the hybrid converter can operate as expected during normal operating conditions and fault conditions. Thus, the composition and control of the H-VSC for OWF integration, transmission are verified and is an alternative to the conventional MMC-HVDC.

REFERENCES

[1] Global Wind Energy Council. *Global Wind Report 2023*. Mar. 27, 2023. [Online]. Available: https://gwec.net/globalwindreport2023/

[2] International Energy Agency. *World Energy Outlook 2023*. Oct. 2023. [Online]. Available: https://origin.iea.org/reports/world-energy-outlook-2023

[3] International Renewable Energy Agency. *WORLD ENERGY TRANSITIONS OUTLOOK 2023: 1.5°C Pathway*. Jun. 2023. [Online]. Available: https://www.irena.org/Publications/2023/Jun/World-Energy-Transitions-Outlook-2023

[4] International Renewable Energy Agency. *Renewable Energy Statistics 2023*. Jul. 2023. [Online]. Available: https://www.irena.org/Publications/2023/Jul/Renewable-energy-statistics-2023

[5] International Renewable Energy Agency. *What are the latest trends in renewable energy?*. Mar. 25, 2023. [Online]. Available: https://public.tableau.com/views/IRENARETimeSeries/Charts?:embed=y&:showVizHome=no&publish=yes&:toolbar=no

[6] E. Pan, B. Yue, X. Li, Z. Zhao, and Q. Zhu, "Integration technology and practice for long-distance offshore wind power in China," *Energy Convers Econ.*, vol. 1, no. 1, pp. 4–19, Oct. 2020.

[7] Z. Li, Q. Song, F. An, B. Zhao, Z. Yu, and R. Zeng, "Review on DC transmission systems for integrating large-scale offshore wind farms," *Energy Convers Econ.*, vol. 2, no. 1, pp. 1–14, Mar. 2020.

[8] H. D. Van, O. Gomis-Bellmunt, and J. Liang, "Wind turbine technologies," in *HVDC Grids: For Offshore and Supergrid of the Future*, 1st ed. Piscataway, NJ, USA: IEEE, 2016, ch. 5, sec. II, pp. 97–108.

[9] SIEMENS. *Siemens revolutionizes grid connection for offshore wind power plants*. Oct. 23, 2015. [Online]. Available: https://www.3blmedia.com/News/Siemens-Revolutionizes-Grid-Connection-Offshore-Wind-Power-Plants

[10] A. Lesnicar and R. Marquardt, "An innovative modular multilevel converter topology suitable for a wide power range," in *Proc. IEEE Bologna Power Tech Conf.*, 2003, vol. 3, Art. no. 6.

[11] M. A. Perez, S. Bernet, J. Rodriguez, S. Kouro, and R. Lizana, "Circuit topologies, modeling, control schemes, and applications of modular multilevel converters," *IEEE Trans. Power Electron.*, vol. 30, no. 1, pp. 4–17, Jan. 2015.

[12] A. Dekka, B. Wu, R. L. Fuentes, M. Perez, and N. R. Zargari, "Evolution of topologies, modeling, control schemes, and applications of modular multilevel converters," *IEEE J. Emerg. Sel. Topics Power Electron.*, vol. 5, no. 4, pp. 1631–1656, Dec. 2017.

[13] J. I. Leon, S. Kouro, L. G. Franquelo, J. Rodriguez, and B. Wu, "The essential role and the continuous evolution of modulation techniques for voltage-source inverters in the past, present, and future power electronics," *IEEE Trans. Ind. Electron.*, vol. 63, no. 5, pp. 2688–2701, May 2016.

[14] Z. Liu, J. Wang, L. Chen, Z. Wang, and Y. Jin, "A time-domain analysis model for modular-multilevel-based grid-forming converters in isolated power supply," *IEEE Trans. Power Electron.*, vol. 38, no. 5, pp. 6259–6271, May 2023.

[15] R. Mallik, B. Majmunović, S. Dutta, G.-S. Seo, D. Maksimović, and B. Johnson, "Control design of series-connected PV-powered grid-forming converters via singular perturbation," *IEEE Trans. Power Electron.*, vol. 38, no. 4, pp. 4306–4322, Apr. 2023.

[16] Y. Zou, L. Zhang, J. Qin, W. Sheng, and Q. Duan, "Phase-unsynchronized power decoupling control of MMC based on feedback linearization," *IEEE Trans. Power Electron.*, vol. 37, no. 3, pp. 2946–2958, Mar. 2022.

[17] J. Wang and P. Wang, "Power decoupling control for modular multilevel converter," *IEEE Trans. Power Electron.*, vol. 33, no. 11, pp. 9296–9309, Nov. 2018.

[18] G. Jia, M. Chen, S. Tang, C. Zhang, and G. Zhu, "Active power decoupling for a modified modular multilevel converter to decrease submodule capacitor voltage ripples and power losses," *IEEE Trans. Power Electron.*, vol. 36, no. 3, pp. 2835–2851, Mar. 2021.

[19] M. Guan, Z. Xu, W. Pan, and Q. Tu, "Analytical calculation of fundamental wave and harmonic characteristics for nearest level modulation," *High Voltage Eng.*, vol. 36, no. 5, pp. 1327–1332, May 2010.

[20] B. Li, R. Yang, D. Xu, G. Wang, W. Wang, and D. Xu, "Analysis of the phase-shifted carrier modulation for modular multilevel converters," *IEEE Trans. Power Electron.*, vol. 30, no. 1, pp. 297–310, Jan. 2015.

[21] Q. Liu, A. Chen, C. Du, and C. Zhang, "A modified nearest-level modulation method for modular multilevel converter with fewer submodules," in *Proc. Chin. Automat. Congr.*, 2017, pp. 6551–6556.

[22] S. S. Thakur, M. Odavic, A. Allu, Z. Q. Zhu, and K. Atallah, "Theoretical harmonic spectra of PWM waveforms including DC bus voltage ripple—Application to a low-capacitance modular multilevel converter," *IEEE Trans. Power Electron.*, vol. 35, no. 9, pp. 9291–9305, Sep. 2020.

[23] Y. Li, X. Shi, B. Liu, F. Wang, and W. Lei, "Maximum modulation index for modular multilevel converter with circulating current control," in *Proc. IEEE Energy Convers. Congr. Expo.*, 2014, pp. 491–498.

[24] J. Peralta, H. Saad, S. Dennetiere, J. Mahseredjian, and S. Nguefeu, "Detailed and averaged models for a 401-level MMC–HVDC system," *IEEE Trans. Power Del.*, vol. 27, no. 3, pp. 1501–1508, Jul. 2012.

[25] L. Yu, R. Li, L. Xu, and G. P. Adam, "Analysis and control of offshore wind farms connected with diode rectifier-based HVDC system," *IEEE Trans. Power Del.*, vol. 35, no. 4, pp. 2049–2059, Aug. 2020.

[26] L. Yu, R. Li, and L. Xu, "Distributed PLL-based control of offshore wind turbines connected with diode-rectifier-based HVDC systems," *IEEE Trans. Power Del.*, vol. 33, no. 3, pp. 1328–1336, Jun. 2018.

[27] Y. Tang, Z. Zhang, and Z. Xu, "DRU based low frequency AC transmission scheme for offshore wind farm integration," *IEEE Trans. Sustain. Energy*, vol. 12, no. 3, pp. 1512–1524, Jul. 2021.

[28] M. M. C. Merlin et al., "The extended overlap alternate arm converter: A voltage-source converter with DC fault ride-through capability and a compact design," *IEEE Trans. Power Electron.*, vol. 33, no. 5, pp. 3898–3910, May 2018.

[29] S. Fan et al., "A cost-effective and DC-fault tolerant alternate arm converter with wide range voltage adaptability," *IEEE J. Emerg. Sel. Topics Power Electron.*, vol. 10, no. 6, pp. 6673–6686, Dec. 2022.

[30] E. M. Farr, R. Feldman, J. C. Clare, and O. F. Jasim, "The alternate arm converter 'extended-overlap' mode: AC faults," *IEEE Trans. Power Electron.*, vol. 36, no. 5, pp. 5371–5388, May 2021.

[31] H. Yang, S. Fan, Y. Dong, H. Yang, W. Li, and X. He, "Arm phase-shift conducting modulation for alternate arm multilevel converter with half-bridge submodules," *IEEE Trans. Power Electron.*, vol. 36, no. 5, pp. 5223–5235, May 2021.

[32] ABB Review Special Report. *60 years of HVDC*. Jul. 2014. [Online]. Available: https://search.abb.com/library/Download.aspx?DocumentID=9AKK106103A8195&LanguageCode=en&DocumentPartId=&Action=Launch

[33] Y. Chang and X. Cai, "Hybrid topology of a diode-rectifier-based HVDC system for offshore wind farms," *IEEE J. Emerg. Sel. Topics Power Electron.*, vol. 7, no. 3, pp. 2116–2128, Sep. 2019.

[34] T. H. Nguyen, D.-C. Lee, and C.-K. Kim, "A series-connected topology of a diode rectifier and a voltage-source converter for an HVDC transmission system," *IEEE Trans. Power Electron.*, vol. 29, no. 4, pp. 1579–1584, Apr. 2014.

[35] R. Li and L. Xu, "A unidirectional hybrid HVDC transmission system based on diode rectifier and full-bridge MMC," *IEEE J. Emerg. Sel. Topics Power Electron.*, vol. 9, no. 6, pp. 6974–6984, Dec. 2021.

[36] D. Holmes and T. Lipo, *Pulse Width Modulation For Power Converters: Principles and Practice*. Hoboken, NJ, USA: Wiley, 2003.

[37] H. Akagi, E. H. Watanabe, and M. Aredes, *Instantaneous Power Theory and Applications to Power Conditioning*. Hoboken, NJ, USA: Wiley, 2007.

[38] H. Wu and X. Wang, "Control of grid-forming VSCs: A perspective of adaptive fast/slow internal voltage source," *IEEE Trans. Power Electron.*, vol. 38, no. 8, pp. 10151–10169, Aug. 2023.

[39] Manitoba Hydro International Ltd. (MHI). HVDC VSC transmission linking an (offshore) islanded wind farm with (onshore) AC grid. Jan. 2022. [Online]. Available: https://www.pscad.com/knowledge-base/article/223

[40] Y. Song and B. Wang, "Survey on reliability of power electronic systems," *IEEE Trans. Power Electron.*, vol. 28, no. 1, pp. 591–604, Jan. 2013.

[41] J. Falck, C. Felgemacher, A. Rojko, M. Liserre, and P. Zacharias, "Reliability of power electronics systems: An industry perspective," *IEEE Ind. Electron. Mag.*, vol. 12, no. 2, pp. 24–35, Jun. 2018.

[42] M. Bennett, N. Dhaliwal, and L. Crowe, "Reliability and availability of HVDC systems," in *High Voltage DC Transmission Systems*, B. R. Andersen and S. L. Nilsson, Eds., CIGRE Green Books. Berlin, Germany: Springer, 2023.

[43] M. Bennett and L. Crowe, "A survey of the reliability of HVDC systems throughout the world during 2017–2018," 2020.

[44] R. Grinberg, G. Riedel, A. Korn, P. Steimer, and E. Bjornstad, "On reliability of medium voltage multilevel converters," in *Proc. IEEE Energy Convers. Congr. Expo.*, 2013, pp. 4047–4052.

[45] C. Kim and S. Lee, "Redundancy determination of HVDC MMC modules," *Electronics*, vol. 4, no. 3, pp. 526–537, 2015.

[46] Y. Tian and G. Konstantinou, “Base failure rate calculation for submodules in modular multilevel converters for mvdc applications,” in *Proc. IEEE 7th Workshop Electron. Grid (eGRID)*, 2022, pp. 1–5.

[47] X. Xie, H. Li, Y. Hu, T. Yang, Y. Wu, and Z. Chai, “Analysis of power loss and reliability on hybrid modular multilevel converter with redundancy configuration for offshore wind turbines,” in *Proc. 22nd Int. Conf. Elect. Machines Syst.*, 2019, pp. 1–6.

[48] S. Isik and S. Bhattacharya, “Reliability and cost modeling of a modular multilevel converter,” in *Proc. IEEE 12th Int. Symp. Power Electron. Distrib. Gener. Syst.*, 2021, pp. 1–8.

[49] P. Kapale and I. Colak, “Reliability and cost figures comparison of modular multilevel converter based on preventive and corrective maintenance,” in *Proc. 10th Int. Conf. Power Electron., Machines Drives*, 2020, pp. 1030–1034.

[50] M. Arifujjaman and L. Chang, “Reliability comparison of power electronic converters used in grid-connected wind energy conversion system,” in *Proc. 3rd IEEE Int. Symp. Power Electron. Distrib. Gener. Syst.*, 2012, pp. 323–329.

[51] K. Pouresmaeil and S. Kaboli, “Reliability analysis of high voltage diode bridge rectifiers to achieve fault tolerance,” in *Proc. 28th Iranian Conf. Elect. Eng.*, 2020, pp. 1–5.

[52] Y. Zhang, H. Wang, Z. Wang, F. Blaabjerg, and M. Saeedifard, “Mission profile-based system-level reliability prediction method for modular multilevel converters,” *IEEE Trans. Power Electron.*, vol. 35, no. 7, pp. 6916–6930, Jul. 2020.

[53] *IEEE Standard for Harmonic Control in Electric Power Systems*, IEEE Standard 519-2022, (Revision IEEE Std 519-2014), Aug. 2022, doi: 10.1109/IEEESTD.2022.9848440.

Chengdong Wang (Student Member, IEEE) received the B.S. degree in electrical engineering and automation in 2007 from Hefei University of Technology, Hefei, China, where he is currently working toward the Ph.D. degree in electrical engineering with the School of Electrical Engineering and Automation.

His current research interests include converter topology and control strategy of high voltage direct current for large scale offshore wind power integration and transmission, and frequency supporting of offshore wind power.

Asif Ali received the bachelor’s degree in electrical engineering from Quaid-e-Awam UEST Nawabshah, Sindh, Pakistan, in 2011 and the master’s degree in electrical engineering from Mehran UET Jamshoro, Sindh, Pakistan, in 2017. He is currently working toward the Ph.D. degree in electrical engineering with the School of Electrical Engineering and Automation, Hefei University of Technology, Hefei, China.

His current research interests include power electronics, novel soft-switching topologies, High-Frequency Link Converters and renewable energy generation technology.

Frede Blaabjerg (Fellow, IEEE) received the Ph.D. degree in electrical engineering from Aalborg University, Aalborg, Denmark, in 1995 and the Honoris Causa degree in engineering from the University Politehnica Timisoara, Timisoara, Romania, in 2017 and Tallinn Technical University, Tallinn , Estonia in 2018.

He was with ABB-Scandia, Randers, Denmark, from 1987 to 1988. He was an Assistant Professor in 1992, an Associate Professor in 1996, and a Full Professor of power electronics and drives in 1998 with AAU Energy. Since 2017, he has been a Villum Investigator. He has authored or coauthored more than 600 journal papers in the fields of power electronics and its applications. He is the co-author of eight monographs and editor of fourteen books in power electronics and its applications, e.g., the series (4 volumes) Control of Power Electronic Converters and Systems published by Academic Press/Elsevier. His current research interests include power electronics and its applications such as in wind turbines, PV systems, reliability, Power-2-X, power quality and adjustable speed drives.

Dr. Blaabjerg was the recipient of 38 IEEE Prize Paper Awards, the IEEE PELS Distinguished Service Award in 2009, the EPE-PEMC Council Award in 2010, the IEEE William E. Newell Power Electronics Award 2014, the Villum Kann Rasmussen Research Award 2014, the Global Energy Prize in 2019 and the 2020 IEEE Edison Medal. He was an Editor-in-Chief for IEEE TRANSACTIONS ON POWER ELECTRONICS, from 2006 to 2012. He has been a Distinguished Lecturer for the IEEE Power Electronics Society, from 2005 to 2007 and for IEEE Industry Applications Society from 2010 to 2011 as well as 2017 to 2018. During 2019–2020, he was the President of IEEE Power Electronics Society. He has been Vice-President of the Danish Academy of Technical Sciences. He is nominated in 2014–2021 by Thomson Reuters to be between the most 250 cited researchers in Engineering in the world.